ADVANCED ELECTRONIC MATERIALS
www.advelectronicmat.de

Transport Spectroscopy of Ultraclean Tunable Band Gaps in Bilayer Graphene

Eike Icking, Luca Banszerus, Frederike Wörtche, Frank Volmer, Philipp Schmidt, Corinne Steiner, Stephan Engels, Jonas Hesselmann, Matthias Goldsche, Kenji Watanabe, Takashi Taniguchi, Christian Volk, Bernd Beschoten, and Christoph Stampfer*

The importance of controlling both the charge carrier density and the band gap of a semiconductor cannot be overstated, as it opens the doors to a wide range of applications, including, for example, highly-tunable transistors, photodetectors, and lasers. Bernal-stacked bilayer graphene is a unique van-der-Waals material that allows tuning of the band gap by an out-of-plane electric field. Although the first evidence of the tunable gap is already found 10 years ago, it took until recent to fabricate sufficiently clean heterostructures where the electrically induced gap can be used to fully suppress transport or confine charge carriers. Here, a detailed study of the tunable band gap in gated bilayer graphene characterized by temperature-activated transport and finite-bias spectroscopy measurements is presented. The latter method allows comparing different gate materials and device technologies, which directly affects the disorder potential in bilayer graphene. It is shown that graphite-gated bilayer graphene exhibits extremely low disorder and as good as no subgap states resulting in ultraclean tunable band gaps up to 120 meV. The size of the band gaps are in good agreement with theory and allow complete current suppression making a wide range of semiconductor applications possible.

1. Introduction

Bernal stacked bilayer graphene (BLG) is a unique material: intrinsically it is a 2D semi-metal, but it can be turned into a 2D semiconductor by applying an external out-of-plane electric field,[1–3] with an electronic band gap that is directly related to the strength of the displacement field. The underlying mechanism of the band gap opening is a textbook example of how the breaking of inversion symmetry results in a gap in the electronic band structure. The first experimental evidence of the tunable band gap in BLG was obtained by angle-resolved photoemission spectroscopy[4,5] and infrared spectroscopy experiments,[6–8] where band gaps up to 250 meV have been reported. Signatures of the tunable band gap have also been observed by scanning tunneling spectroscopy[9,10] and in early transport measurements.[11–21] However, in the latter experiments, subgap states caused by disorder made it impossible to completely suppress the electron conduction,[22] making such BLG devices not suitable for semiconductor applications.

This shortcoming was solved neither by fabricating double-gated structures based on suspended BLG[23–26] nor by encapsulating BLG into hexagonal boron nitride (hBN).[27–30] Only recently, with the use of graphite gates, the fabrication technology has advanced to the level where it is possible to open a gate-controlled band gap that results in a true band insulating state in BLG.[31,32]

Here, we exploit this fabrication technology and show that the tunable band gap of BLG can finally, also directly, be observed in finite bias transport spectroscopy measurements. The obtained band gaps are in good agreement with theory

E. Icking, L. Banszerus, F. Wörtche, F. Volmer, P. Schmidt, C. Steiner, S. Engels, J. Hesselmann, M. Goldsche, C. Volk, B. Beschoten, C. Stampfer
JARA-FIT and 2nd Institute of Physics
RWTH Aachen University
52074 Aachen, Germany
E-mail: icking@physik.rwth-aachen.de

The ORCID identification number(s) for the author(s) of this article can be found under https://doi.org/10.1002/aelm.202200510.

DOI: 10.1002/aelm.202200510

E. Icking, L. Banszerus, P. Schmidt, C. Steiner, S. Engels, M. Goldsche, C. Volk, C. Stampfer
Peter Grünberg Institute (PGI-9)
Forschungszentrum Jülich
52425 Jülich, Germany

K. Watanabe
Research Center for Functional Materials
National Institute for Materials Science
1-1 Namiki, Tsukuba 305-0044, Japan

T. Taniguchi
International Center for Materials Nanoarchitectonics
National Institute for Materials Science
1-1 Namiki, Tsukuba 305-0044, Japan

as well as with the values extracted from thermally activated transport.[16–21,29,30] Most interestingly, we use finite bias spectroscopy, to systematically compare different double-gated BLG/hBN device technologies, as this method allows to sensitively probe hopping-transport due to potential disorder or impurity states, which both can result in effective subgap and tail states. The investigated devices differ mainly in the bottom gate material (graphite, gold, or highly doped silicon) and in the corresponding fabrication process. We show that the fabrication technology sensitively impacts the maximum device resistance and the presence and outline of diamonds of strongly suppressed conductance for finite bias voltage when measuring transport through electrostatically gapped BLG, as well as the tunability of the band gap with the electric displacement field.

We find that BLG devices with a graphite gate behave very closely to what theory predicts for ideal BLG, showing a truly semiconducting behavior in the presence of an applied displacement field. In the gapped regime, we measure maximum resistance values on the order of 100 GΩ (limited only by the measurement setup), and we observe no appreciable signature of trap or impurity states with subgap energy. In contrast, both silicon and gold-gated devices appear to be affected by subgap states and disorder, but to different degrees. While very high gap-induced resistances are still observed in gold-gated devices, where the band gap just appears to be reduced in finite bias measurements, no gap can be directly observed in silicon-gated devices. All this confirms that the intrinsic properties of BLG become exploitable in graphite-gated BLG/hBN heterostructures, which therefore represents the most promising platform to unleash the potential of this unique tunable 2D semiconductor with interesting applications for THz electronics, quantum technologies, and mesoscopic physics.

2. An Electrostatically Tunable Band Gap

The inversion symmetry and its controlled breaking play an important role in determining the properties of intrinsic and gapped BLG. In the intrinsic form, the orbitals of the carbon atoms A1 and B2, which are responsible for the low energy spectra of BLG, are inversion-symmetric, and BLG is a semimetal (see **Figure 1**a,b).[2,3] The symmetry is broken in the presence of an external out-of-plane displacement field, which induces an onsite potential difference Δ between the upper and lower graphene layer. This potential difference leads in turn to the appearance of a band gap between the conductance and the valence band,[1–3] as illustrated in Figure 1b. The size of the band gap, E_g, depends on the onsite potential difference Δ as[2,3]

$$E_g(\Delta) = \frac{|\Delta|}{\sqrt{1+(\Delta/\gamma_1)^2}} \tag{1}$$

where $\gamma_1 \approx 0.38$ eV is the interlayer coupling strength.[33,35–37] The dependence between Δ and the external electric displacement field is however non-trivial, as Δ depends also on the screening of the charge carriers on the layers of BLG, which is influenced in turn by the onsite potential difference Δ, thus requiring a self-consistent analysis.[3,34]

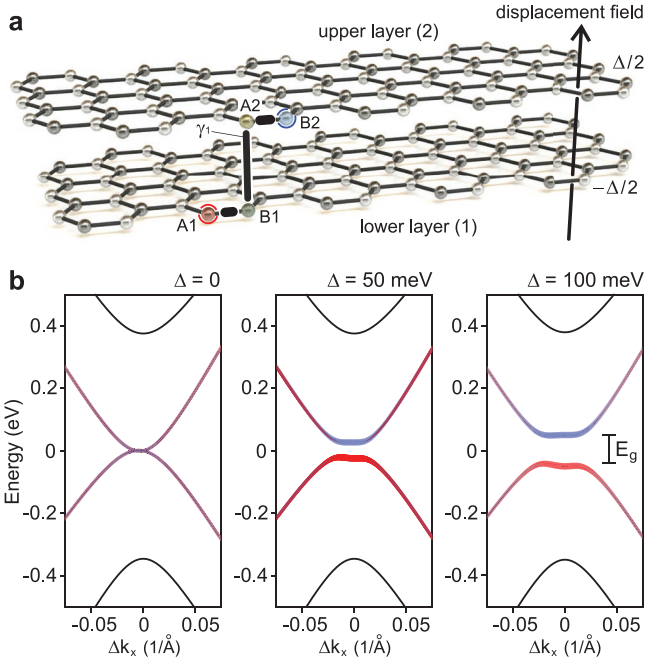

Figure 1. a) Schematic illustration of Bernal-stacked bilayer graphene. An out-of-plane electric displacement field results in the onsite potential difference Δ between the layers, which breaks the inversion symmetry. The atomic orbitals of atoms A1 and B2 (highlighted in red and blue) determine the low energy spectra. b) Electronic band structure of BLG near the K-point, calculated according to Equation (30) in ref. [33] for zero on-site potential difference (left panel), Δ = 50 meV (central panel), and Δ = 100 meV (right panel). The projection on the $2p_z^A1$ and $2p_z^B2$ -orbitals are highlighted in blue and red, respectively.

Different models have been used to calculate the dependence of the interlayer asymmetry Δ on the applied out-of-plane displacement field D, either using a simple plate-capacitor model with Hartree screening[1,3] or, more recently, by additionally taking into account the layer-dependent out-of-plane polarization of the carbon orbitals.[34] In both cases Δ can be expressed as

$$\Delta = \frac{d_0 e D}{\varepsilon_0 \varepsilon_z} + \frac{d_0 e^2}{2\varepsilon_0 \overline{\varepsilon}} \delta n(\Delta) \tag{2}$$

where $d_0 = 0.34$ nm is the interlayer spacing of BLG, e is the (magnitude of the) elementary charge, and $\varepsilon_z, \overline{\varepsilon}$ are effective dielectric constants. In the model of ref. [1,3], $\varepsilon_z = \overline{\varepsilon} = \varepsilon_{BLG}$, where $\varepsilon_{BLG} \approx 2$ is the effective dielectric constant of BLG.[38–40] In contrast, in ref. [34] ε_z is the effective out-of-plane dielectric susceptibility of graphene and $\overline{\varepsilon} \equiv 2/(1+\varepsilon_z^{-1})$. Finally, $\delta n(\Delta)$ is the difference between the charge carrier density in the upper and lower layer, whose detailed expression also depends on the considered model (see Supporting Information). Below we will make use of both models when comparing theory with experiment.

2.1. Double-Gated BLG Devices

Experimentally, the way to apply an out-of-plane electric field to BLG and to control independently its chemical potential is to

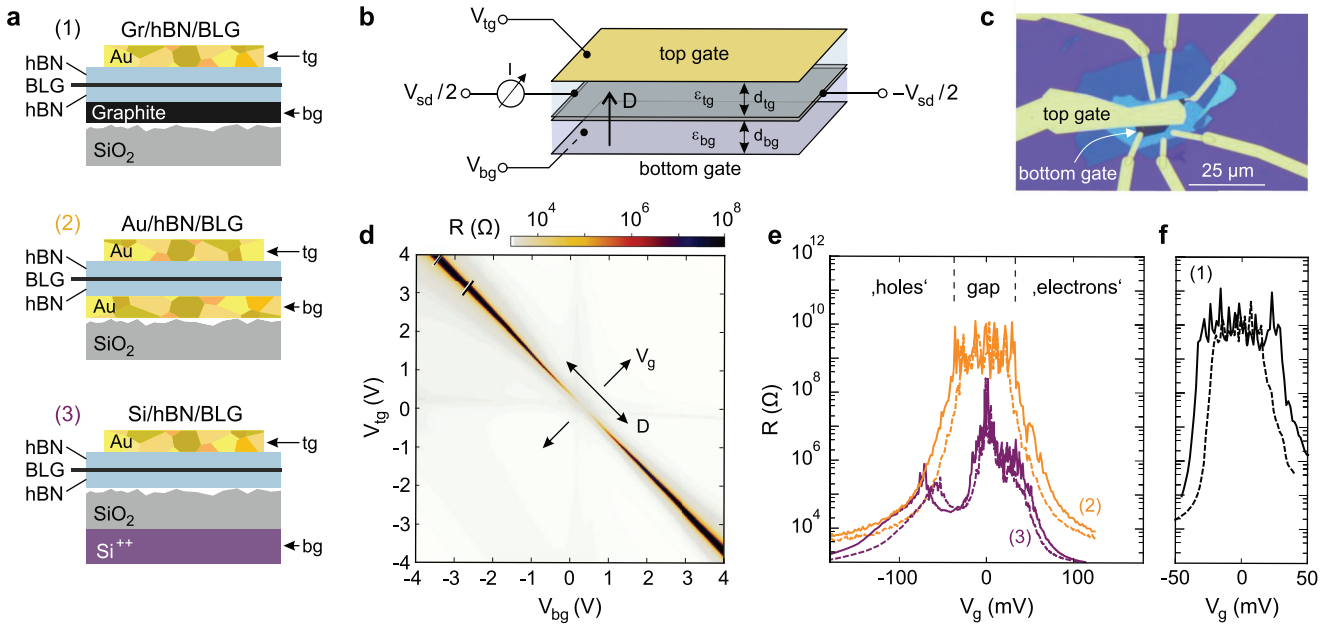

Figure 2. a) Schematic cross-sections of the three types of double-gated BLG devices (class 1–3) investigated in this work. All devices have a gold top gate (tg) but different bottom gates (bg). b) Illustration of a generic double-gated BLG device consisting of a top gate and a bottom gate and of the contacting scheme. c) Optical image of an Au/hBN/BLG device. d) Two-terminal resistance of the device shown in panel (c) as a function of V_{bg} and V_{tg} at T = 1.6 K and V_{sd} = 1 mV. e) Resistance of the Au/hBN/BLG device (orange lines) and of the Si/hBN/BLG device (purple lines) measured at T = 1.6 K and V_{sd} = 2 mV along the direction of the short black lines in panel (d). These lines correspond to displacement fields D = –0.58 V nm^{-1} and D = –0.48 V nm^{-1} for the Au/hBN/BLG device (solid and dashed orange line, respectively), and to D = –0.56 V nm^{-1} and D = –0.48 V nm^{-1} for the Si/hBN/BLG device (solid and dashed purple line, respectively). f) Same type of measurement as in panel (e) for a Gr/hBN/BLG device, for displacement fields D = –0.54 V nm^{-1} (solid line) and D = –0.46 V nm^{-1} (dashed line).

embed it into a plate capacitor, that is, to have a bottom and a top gate (see **Figure 2**a,b).

In this work, we compare devices fabricated with three different technologies. All devices are based on BLG encapsulated into hBN and have a metallic top gate (tg), but differ in the bottom gate (bg), as illustrated in Figure 2a. Specifically, we consider devices with a graphite bottom gate (referred to as "Gr/hBN/BLG" or class 1 devices), devices with a gold (Au) bottom gate (referred to as "Au/hBN/BLG" or class 2 devices), and devices that use the heavily doped silicon substrate as bottom gate (referred to as "Si/hBN/BLG" or class 3 devices). An optical image of a final device with an Au bottom gate based on a stack-flipping process is shown in Figure 2c. It is worth noting here that although the Au gate/stack-flipping process results in less disorder than directly placing an hBN/BLG/hBN stack on a (rough) Au bottom gate, the Au top gate (used in all devices) has overall less detrimental effect on device quality, which is due to the fact that the BLG heterostructure no longer needs to be moved afterward. Details on the device fabrication are given in the Supporting Information.

In the investigated devices, the top gate is narrower than the bottom gate, and the BLG regions doped exclusively by the bottom gate act as leads. In the double-gated region, the voltages V_{tg} and V_{bg} applied to the top and to the bottom gate induce a displacement field D through the BLG

$$D = \frac{e}{2}\left[\alpha_{bg}\left(V_{bg} - V_{bg}^{0}\right) - \alpha_{tg}\left(V_{tg} - V_{tg}^{0}\right)\right] \tag{3}$$

where V_{tg}^{0}, V_{bg}^{0} are the offset of the charge neutrality point (CNP) from $V_{tg} = V_{bg} = 0$, and $\alpha_{tg} = \varepsilon_0\varepsilon_{tg}/(ed_{tg})$ and $\alpha_{bg} = \varepsilon_0\varepsilon_{bg}/(ed_{bg})$ are the lever-arms determined by the capacitive coupling of the top and bottom gate, respectively (ε_{tg}, ε_{bg} are the dielectric constants and d_{tg}, d_{bg} the thicknesses of the dielectric layers; see Figure 2b). The effect of the voltages V_{tg} and V_{bg} on the chemical potential in the double-gated region is understood at best in terms of the effective gate voltage

$$V_g = \frac{(V_{bg} - V_{bg}^{0}) + \beta(V_{tg} - V_{tg}^{0})}{1+\beta} \tag{4}$$

where $\beta = \alpha_{tg}/\alpha_{bg}$ is the ratio of the two lever-arms. This effective gate voltage is defined such that V_g is directly linked to the electro-chemical potential via $\mu \approx e\,V_g$, as long as μ is within the band gap. Also V_g allows to change the total charge carrier density n outside the band gap by $\Delta n \approx (\alpha_{tg} + \alpha_{bg})\Delta V_g$, if both layers are on the same potential (for more details see Supporting Information). For all devices, we extract the values of V_{tg}^{0}, V_{bg}^{0}, and β from resistance-map measurements, and the value of either α_{tg} or α_{bg} from quantum Hall measurements[41–43] (see Supporting Information).

2.2. Resistance Maps and Maximal Resistance

As a first step to characterize the double-gated BLG devices, we record resistance maps like the one of Figure 2d, by applying

a small source–drain bias V_{sd} and by measuring the current I as a function of V_{tg} and V_{bg} (see schematic in Figure 2b). The resistance maps exhibit two distinct features: i) A diagonal line of elevated resistance R, which marks the shifting of the charge neutrality point of the BLG in the double-gated region as a function of V_{tg} and V_{bg}. This line represents the $V_g = 0$ axis (i.e., $\mu = 0$). The slope of this line is directly given by the ratio of the lever arms $\beta = \alpha_{tg}/\alpha_{bg}$. For example, for the measurement shown in Figure 2d, it is $\beta = 0.99$, indicating a very symmetric capacitive coupling of the top and bottom gate.

ii) Along this diagonal line the maximum resistance R_{max} strongly increases while increasing the magnitude of the displacement field, which is a hallmark of the opening of the band gap induced by the displacement field.

While these qualitative features are common to the resistance maps performed on devices of all three different classes (for a comparison of carrier mobilities see Supporting Information), the differences between the three technologies become apparent when comparing line traces of the resistance measured as a function of V_g at fixed D-fields, see Figure 2e,f. In all cases, we observe an abrupt decrease of the largest resistance around $V_g = 0$. But, while devices with a graphite and gold bottom gate show well-defined plateaus of high resistance (see Figure 2f and orange traces in Figure 2e), the resistance of the device with a silicon bottom gate is significantly lower and varies by more than three orders of magnitude within the gate voltage range where the band gap is expected (purple traces in Figure 2e). These strong variations and the reduced maximum-resistance can be explained in terms of hopping transport through subgap states caused by the disorder due to charged impurities in the SiO_2, at the SiO_2/hBN interfaces, or at the unscreened BLG edges[11,16–19,21,27] which create spatial electrostatic variations along the transport channel and are the main origin of the observed disorder potentials (see also discussion in Section 3. Vice versa, the high-resistance plateaus observed in devices with graphite or a gold bottom gate suggest that the chemical potential is tuned through a clean band gap, with few or no subgap states. For both types of devices, the width of the high-resistance plateau—that is, the size of the band gap—increases as expected with increasing displacement field (see dashed and solid resistance traces in Figure 2e,f). However, devices with a graphite bottom gate exhibit a much sharper onset of the plateau and slightly higher values of resistance than those with a gold bottom gate, indicating that graphite gates are more effective than metallic ones at suppressing residual charge transport through the band gap and particularly near the band edges. This difference can be attributed to the disorder, that is, spatial electrostatic variations along the BLG transport channel, caused: i) by the fabrication process of the Au-gated devices, which is more prone to interface contamination; or (ii) ultimately by grain boundaries in the gold itself.[44]

The different performance of the three technologies becomes even more apparent by plotting the maximum resistance R_{max} as a function of the displacement field D, see **Figure 3**a (for more details on why R_{max} is a good quantity, see Supporting Information). In this plot, we report both data from three devices measured in our lab (colored data points), as well as data taken from literature (open data points). This overview plot shows that the maximum resistance attainable for a given value of D strongly depends on the fabrication technology used for the double-gated BLG devices. Devices, where BLG is directly placed on SiO_2, require high displacement fields ≈1.6 V nm^{-1} to reach moderate values of $R_{max} \approx 1$ MΩ.

Encapsulating BLG between hBN layers already helps reducing the disorder potential and allows achieving maximum resistances in the range of 100 MΩ − 1 GΩ at D-fields of around $|D| \approx 0.6$ V nm^{-1} (and a temperature of $T \approx 1.5$ K). The observed saturation of R_{max} for higher D-fields can be explained by disorder-induced hopping transport at subgap energies and along the edges of the BLG.[11,16–19,21,27] The use of a metallic gate allows to reach values of R_{max} as high as 10 GΩ at moderate values of D, but it is only the use of a graphite gate that allows to open a real clean band gap and to completely suppress the current at reasonably low D-fields, reaching $R_{max} \approx 100$ GΩ—which represents also the maximum value of resistance measurable in our experimental setup. The values of R_{max} measured in our Gr/hBN/BLG device compare well with the data of refs. [31,32] and, at low D-fields, also with the values measured in a double-gated suspended BLG device (see diamond symbols in Figure 3a, taken from ref. [23]).

2.3. Thermally Activated Transport

The maximum resistance is, of course, a function of temperature. For the three devices illustrated in Figure 2a, we study the maximum resistance R_{max} as a function of temperature for a fixed value of the displacement field D. To extract information on the underlying transport mechanisms, we plot R_{max} logarithmically as a function of T^{-1}, as shown in Figure 3b.

At low temperatures, $T < 10$ K ($T^{-1} > 0.1$ K^{-1}), R_{max} only weakly depends on $1/T$, as predicted by both variable range hopping (VRH)[17,20] and a combination of nearest-neighbor hopping and VRH.[18,30] In this regime, the values of R_{max} observed for the three gating technologies that differ by several orders of magnitude. The low resistance values at low temperature of the Si/hBN/BLG sample are reminiscent of those observed in disordered semiconductors,[45] where transport via impurity bands and hopping transport dominates. This notion is also in agreement with earlier studies[16,21] and with compressibility measurements,[46,47] which have shown that there is a large density of (localized) states in gapped BLG when placed on SiO_2, resulting in low values of R_{max}.

At high temperatures $T > 40$ K ($T^{-1} < 0.025$ K^{-1}), for all types of devices the dependence of R_{max} on $1/T$ is well described by thermally activated transport,[16–21,29,30] that is, $R_{max} \propto \exp(E_g/(2k_BT))$, where E_g is the band gap energy and k_B the Boltzmann constant. By fitting a line to the resistance data in the Arrhenius plot (see, e.g., dashed line in Figure 3b) we can extract E_g at a given value of D for the different devices. Repeating this type of fitting for different values of D, we obtain the plot shown in Figure 3c. It can be observed, that the values of E_g determined in this way for the different devices agree rather well with each other, independently of the fabrication technology. This is the case because at high temperatures the impact of localized subgap states is eventually smeared out by thermal excitations.

Our data also agree well with the band gaps reported by earlier experiments (see opens symbols and crosses in Figure 3c)[8,17,30]

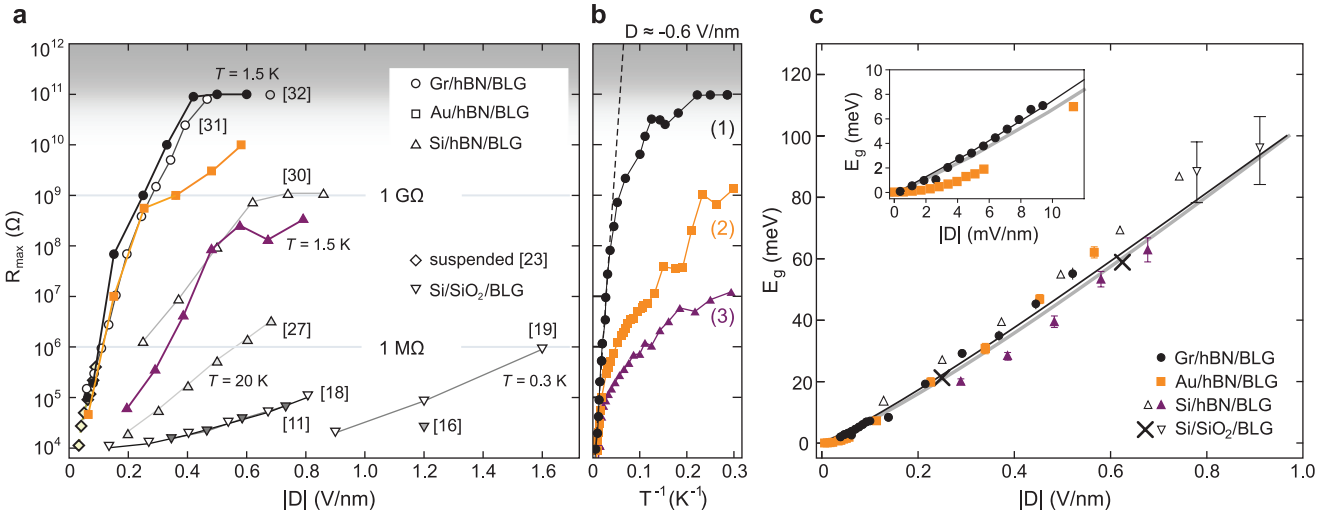

Figure 3. a) Maximum resistance (R_{max}) as a function of displacement-field for 12 different devices based on different gating technologies (see labels). This plot include both data from the devices investigated in Figure 2 (colored data points, same color code as in Figure 2e,f), as well as data from literature. The dark gray area shows resistance values that are not measurable with our experimental setup. Therefore only a lower limit can be given. b) Arrhenius plot showing the maximum resistance R_{max} of the three devices investigated in Figure 2e,f as a function of the inverse temperature $1/T$ at a constant D-field (same labeling as in Figure 2e,f, and panel (a)). The black dashed line corresponds to a fit of the maximum resistance assuming thermal activated transport $R_{max} \propto \exp(E_g/(2k_BT))$. c) Band gap energy E_g as function of the displacement field. The data points correspond to the values of E_g extracted by fitting the high-temperature regime of the Arrhenius plot. The black line indicates the values of E_g predicted by the model of McCann and Koshino,[3] the gray line shows the solution of a simplified model by ref. [34] with $\varepsilon_z = 1.65$ (see Supporting Information). The black crosses are taken from ref. [8], the open downward-pointing triangles from ref. [17] and the open upward-pointing triangles from ref. [30]. The inset shows a close-up for small D-fields.

and with the values predicted by theory. Here, we consider both the self-consistent solution of the plate-capacitor model with Hartree screening proposed by McCann and Koshino[3] with $\varepsilon_{BLG} = 2$ (black line in Figure 3c), as well as the more recent model of ref. [34], which takes into account the layer-dependent polarization of the orbitals (gray line). In this case, we used $\varepsilon_z = 1.65$ for the effective out-of-plane dielectric susceptibility of graphene, see Equation (2). For the device with graphite back gate, the extracted values of E_g agree well with theory even at very low displacement fields (see inset in Figure 3c).

3. Direct Observation of the Band Gap

Measurements like those presented in Figure 3b,c allow to extract the size of the electrostatically induced band gap, E_g, but not to observe it directly. To directly probe the band gap, we use finite-bias spectroscopy at low temperatures, that is, we measure the differential conductance of our devices, $g = dI/dV_{sd}$, as a function of V_g and of V_{sd}. This is a sensitive method to probe the characteristic energy scales of a system and the presence of localized states.

Figure 4a shows finite-bias spectroscopy measurements performed at $T = 50$ mK in a device with a graphite gate, for different values of the displacement field D. Diamond-shaped regions of strongly suppressed conductance can be observed around $V_g = V_{sd} = 0$, where the size of the diamond scales with the applied D-field. For large values of D, the extent of the region of strongly suppressed conductance along the V_{sd} axis agrees very well with the size of the band gap predicted by theory, represented here by the horizontal white dashed lines.

The schematics of Figure 4b depict different characteristic regimes that correspond to the points marked with A, B, C in the rightmost panel of Figure 4a. Point A represents the condition of $V_{sd} = V_g = 0$ at the center of the diamond, where charge transport through the device is suppressed the most. Point B represents the onset of charge transport induced by tuning V_g such that the conduction band in the double-gated area of the device is aligned with the conduction band of the leads. Point C represents the onset of conduction caused by a sufficiently large source–drain bias voltage applied symmetrically over the gated region (i.e., $\pm V_{sd}/2 = \pm E_g/(2e)$). The source–drain voltage creates a p–n junction within the BLG, over which the complete V_{sd} drops as long as there is no current flowing (for more details see Supporting Information). This results in the diode-like behavior of the bias-dependent current shown in Figure 4c, where the threshold voltage clearly depends on the D-field and therefore on the size of the band gap.

Please note that the slight asymmetries in dI/dV_{sd} outside the diamonds with respect to V_{sd} and V_g (see e.g., white arrow in the fourth panel of Figure 4a) can be explained by the D-field dependent layer polarization and a spatially varying disorder potential. For example, for negative displacement field the carriers near the valance band edge ($V_g < 0$) are located in the upper BLG layer[3,48] (see Figure 1b), which is closer to the Au top gate. Thus, the asymmetry in V_g indicates asymmetries in the residual disorder at the Au top and graphite bottom gate interface. The asymmetry in V_{sd} indicates a spatial variation of disorder, as the location of the p–n junction underneath the top gate in this case depends on the polarity of V_{sd} (for more details, see Supporting Information).

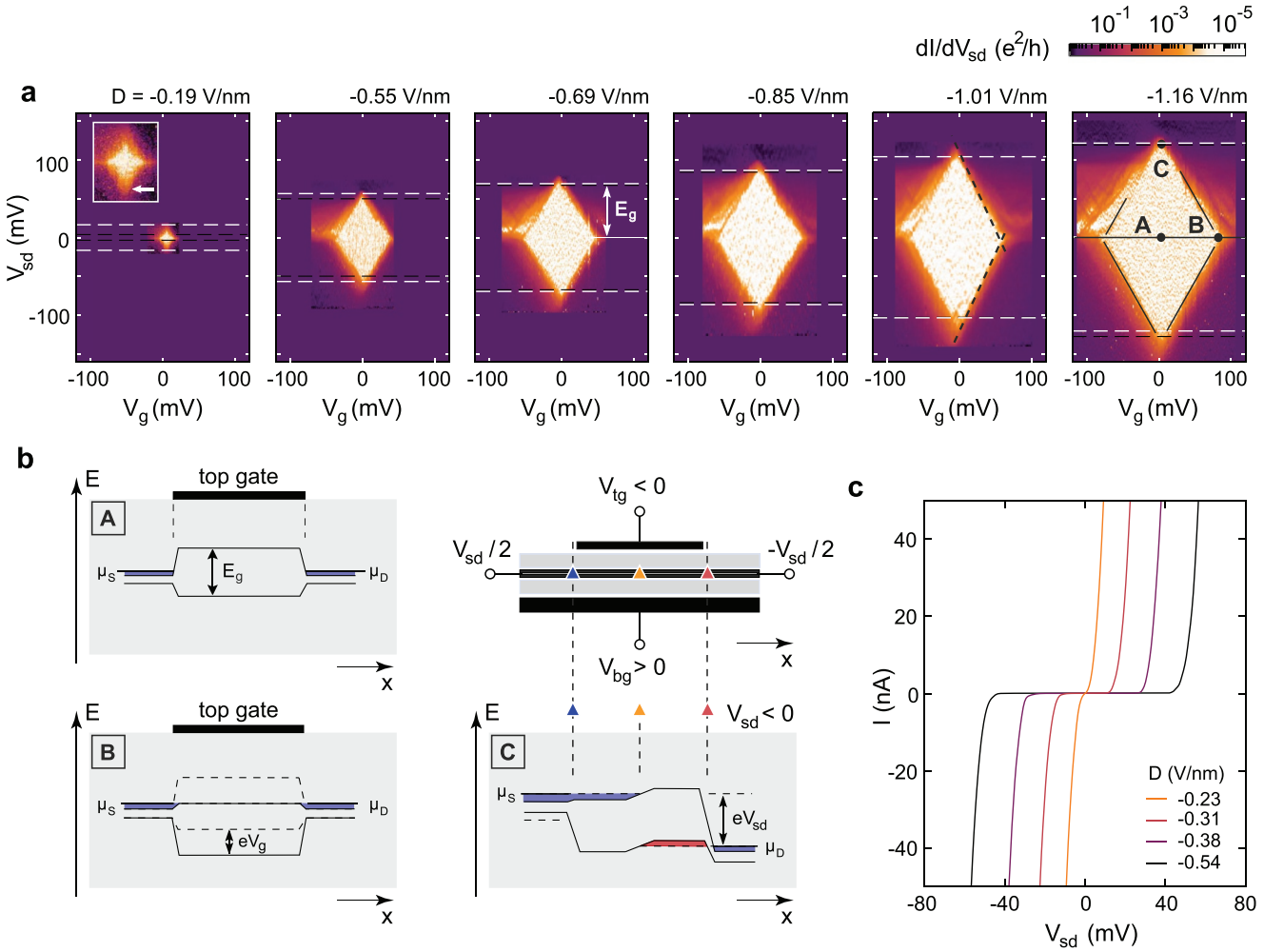

Figure 4. a) Color plot of the differential conductance dI/dV_{sd} of a Gr/hBN/BLG device, measured at $T = 50$ mK as a function of V_{sd} and V_g for different displacement fields (see labels). The white dashed-lines denote the band gap predicted by the model of ref. [3] (for $\varepsilon_z = \overline{\varepsilon} = \varepsilon_{BLG} = 2$), the black dashed lines denote the effective gap E_g^{eff} extracted as described in the main text. The inset shows a magnification for $D = -0.19$ V nm^{-1}. Even at small displacement fields, the area of suppressed differential conductance presents a pronounced diamond shape. b) Schematic representation of the various transport regimes at the points labeled as A, B, C in the rightmost diamond in panel (a). At $V_{sd} = 0$ and $V_g = 0$, transport is strongly suppressed by the presence of a band gap in the double-gated region (A). Transport is re-established either by changing the chemical potential in the double-gated region using the effective gate voltage V_g (B) or by applying a sufficiently large source–drain voltage V_{sd}, which changes the effective potential at the edges of the double-gated BLG, introducing charge carriers and forming a p–n junction. c) *I*–*V* characteristic of the Gr/hBN/BLG device for different values of D at constant V_g. The device shows a clear diode-like behavior, with no appreciable sub-threshold current.

Figure 5a–c presents the same type of bias-spectroscopy measurements performed at $T = 1.6$ K on a second device with a graphite bottom gate (Figure 5a), as well as on a device with gold bottom gate (Figure 5b) and on one with silicon bottom gate (Figure 5c). Also at this higher temperature, the device with graphite bottom gate shows at large D-fields a well-defined diamond-shaped region of strongly suppressed conductance around $V_g = V_{sd} = 0$, whose span along the V_{sd} axis is in fairly good agreement with the size of the band gap predicted by theory (horizontal white dashed lines).

The slopes of the diamond outlines in the $V_{sd} - V_g$ map is very close to two as highlighted by the dashed lines (see also the second rightmost panel in Figure 4a). In Figure 5d we show the extracted outline of the diamond (resistance threshold value of 10^9 Ω) for two different displacement fields (see labels). In both cases, the slope agrees very well with a slope of two (see gray lines). This means that V_g indeed tunes directly the chemical potential $\mu = eV_g$ in the band gap region and no trap states need to be charged. The slope of two results from the fact that when starting in configuration A (see Figure 4a,b) we need either $eV_{sd} = E_g$ to lift the band gap (moving to point C) or $\mu = E_g/2 = eV_g$ (moving to point B) resulting in $\Delta V_{sd} = 2\Delta V_g$.

The fact that this can be observed, in turn, unambiguously indicates the absence of impurity bands, localized states or any other trap state that can potentially be charged in the device.

The device with a gold bottom gate presents also a region of strongly suppressed conductance for large D-fields. However, this does not appear as a single, well-defined diamond, but as a series of overlapping diamonds with different sizes and positions (see right panel of Figure 5b). The device with silicon bottom gate shows overall much higher conductance, with no clear feature that can be related to the band gap energy (Figure 5c).

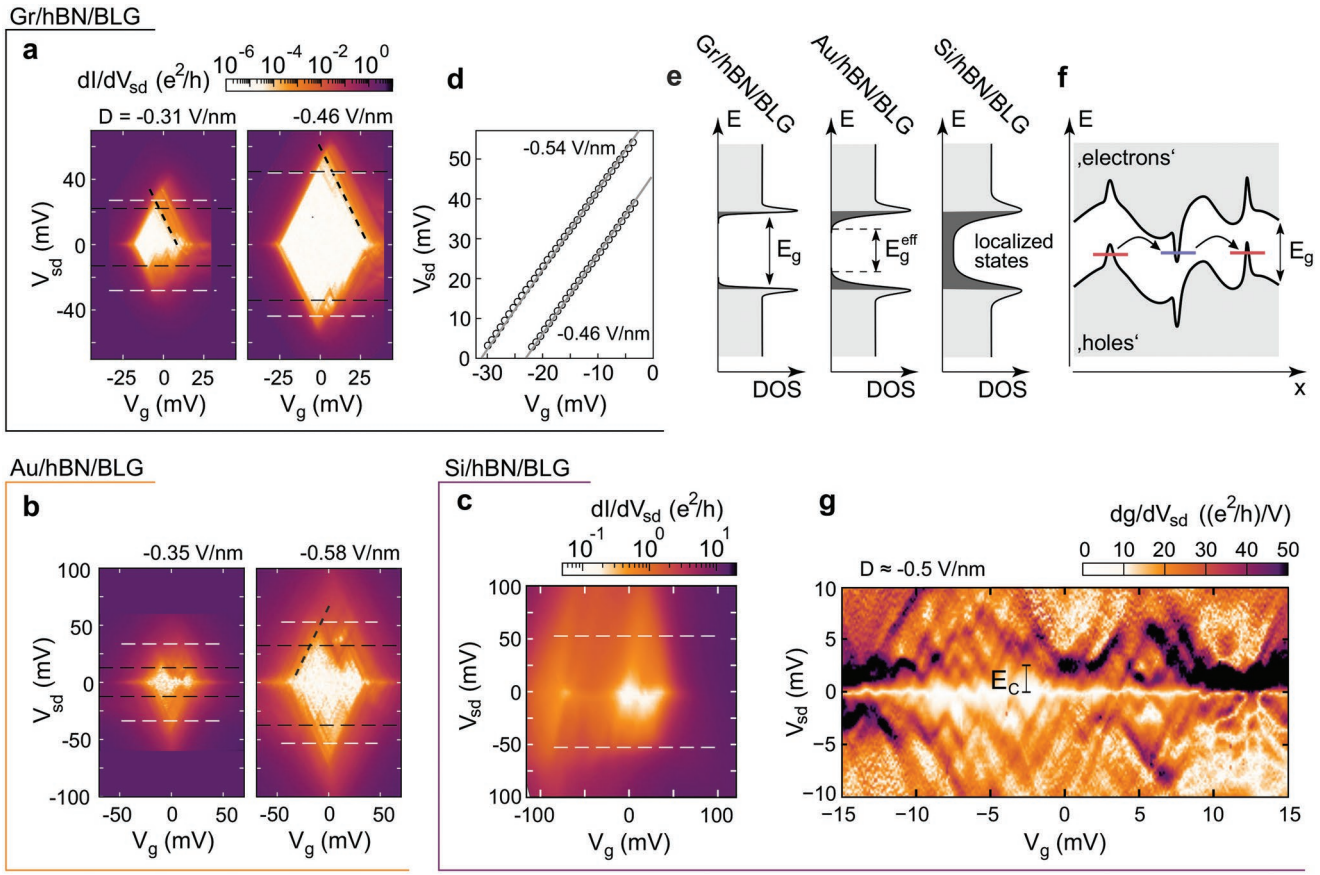

Figure 5. a,b) Color plots of the differential conductance of a (second) Gr/hBN/BLG device (a) and of a Au/hBN/BLG device (b), measured as a function of V_{sd} and V_g at 1.6 K for different displacement fields. As in Figure 4a, the dashed white lines indicate the size of the band gap as predicted by the model of ref. [3]; the horizontal black-dashed lines the size of the effective gap, E_g^{eff}, extracted as discussed in the main text. The diagonal black-dashed lines have a slope of two. c) Differential conductance of a Si/hBN/BLG device, measured at 1.6 K and $D = -0.5$ V nm^{-1}. No clear feature related to the band gap can be observed. d) Extracted diamond edge (threshold resistance 10^9 Ω) for two different D-fields (see labels). The gray lines have a slope of exactly two. e) Schematics of the density of states (DOS) in the three different types of BLG devices. Disorder-induced localized states give rise to tail states with subgap energies that reduce or effectively close the band gap. f) Schematic representation of the band gap of a Si/hBN/BLG device. The presence of strong potential disorder gives rise to localized states with subgap energies, leading to hopping transport through the band gap. g) Derivative of the differential conductance $g = dI/dV_{sd}$ for small V_{sd}. The diamond-like features can be associated to localized electronic states or charge islands with charging energy $E_C \approx 2-3$ meV.

As already discussed in Section 2, the different behavior of the three devices can be traced back to their different level of disorder. In the device with a silicon bottom gate, the unscreened potential of charges trapped in the SiO_2 substrate or at the SiO_2/hBN interfaces creates localized states with subgap energies,[49–54] as sketched in Figure 5e,f. Signatures of hopping transport can indeed be found in the derivative of the differential conductance dg/dV_{sd}, see Figure 5g. Here, we observe diamond-like features associated to the charging of charge islands or of individual localized states, as characteristic for statistical Coulomb blockade.[55,56] The extent of these diamond features in V_{sd} is related to the characteristic charging energy E_C of a localized state, a charge puddle, or to the energy spacing between different states. Here, we find typical energies in the range of 2–3 meV. The observation of individual charging events indicates that the total number of localized states (or puddles) contributing to transport is rather limited. Nevertheless, these states provide a percolation channel through the gated BLG region and prevent a complete current suppression, in good agreement with earlier reports.[18,19,21,30]

The presence of a local bottom gate—either of gold or graphite—strongly screens the disorder potential caused by charged impurities and allows to open a real band gap in BLG by means of a displacement field. However, the band gap is ultraclean only in the case of devices with a graphite gate, while the device with a gold gate still presents signatures of transport through localized states with subgap energies. The presence of these localized states results in tail states in the density of states (DOS), which reduce or—in the case of silicon-gated devices—effectively suppress the band gap (see schematics in Figure 5e).

To quantitatively compare the band gaps observed by transport spectroscopy with theory, we define the effective band gap $E_g^{eff} = e(V_{sd}^+, th + |V_{sd}^-, th|)/2$, where $V_{sd}^{\pm}, th$ are the values of V_{sd} at which the differential conductance is equal to $(dI/dV_{sd})_{th} = 10^{-9}$ S at $V_g = 0$. These threshold voltages are indicated as dashed black lines in Figures 4a and 5a,b. Note

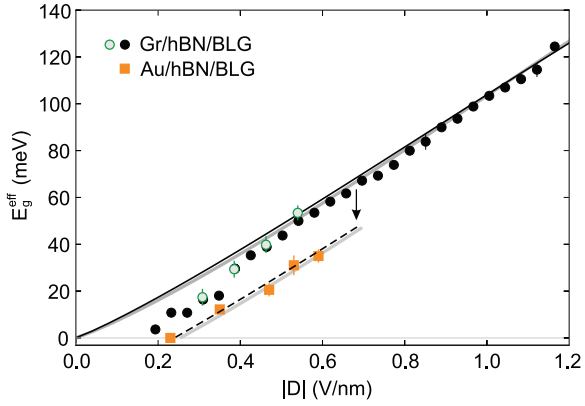

Figure 6. Comparison between the effective values of the band gap E_g^{eff} extracted by transport spectroscopy measurements and the values of E_g predicted by theory (black line: model of ref. [3], gray line: simplified model of ref. [34] with $\varepsilon_z = 1.65$). The overall good agreement between theory and the value of E_g^{eff} extracted from the Gr/hBN/BLG devices (black circles from device #1 (Figure 4a); green circles from device #2 (Figure 5a,d)) indicate that these devices are only affected by very weak residual potential-disorder. Vice versa, the discrepancy observed for the Au/hBN/BLG device (orange squares) indicates the presence of disorder-induced tail states, as sketched in Figure 5e.

that the differential conductance of the Si/hBN/BLG device is always higher than 10^{-9} S. **Figure 6** shows the values of the effective gap E_g^{eff} as a function of the displacement field D for two devices with a graphite bottom gate and for one with a gold bottom gate. For the devices with a graphite bottom gate, we observe an excellent agreement between the band gap measured by transport spectroscopy, E_g^{eff}, and the values predicted by theory for D-fields larger than 0.3 V nm^{-1}. The deviations at smaller values of D indicate the presence of some residual disorder, whose influence is larger for small band gaps (see also inset of the leftmost panel in Figure 4a). Vice versa, for the device with a gold bottom gate the effective transport gap E_g^{eff} is around 20 meV smaller compared to the expected values. This confirms the presence of extended tail states within the band gap, as sketched in Figure 5e. As for all devices the preparation of the BLG has been the same, rather than impurities or defects related to the BLG, these tail states are most likely induced by substrate roughness, or by contaminations at the interfaces due to the fabrication process of the gold-gated device[57–59] or by the disorder caused by grain boundaries in the gold[44] and are not caused by impurities or edge states in the BLG itself.

4. Summary and Outlook

To conclude, we showed that finite-bias spectroscopy is a versatile method to characterize the band gap in BLG. Its high sensitivity allows comparing the influence of (electrostatic) disorder potentials for different gating-technologies. The measurements clearly indicate that devices with a graphite bottom gate fabricated as part of the van-der-Waals heterostructure outperform devices with gold and Si/SiO_2 gates, and behave very closely to what theory predicts for ideal BLG. In graphite-gated devices, we achieve band gaps of about 120 meV with resistances up to 100 GΩ within the band gap (only limited by the setup). These results underline the importance of graphite as a bottom gate for BLG-based van-der-Waals heterostructures.

The high quality of Gr/hBN/BLG devices demonstrated in this work allows to readdress the broad field of possible applications offered by BLG, such as diodes,[60] phonon-lasers,[35,61] hot-electron bolometers,[62] field-effect transistors (FET),[63–65] and tunnel FETs.[66] The latter two are especially interesting for terahertz (THz) detection, where graphene and BLG based devices have already shown promising results.[67,68] The low disorder of Gr/hBN/BLG technology offers the possibility of significantly improving the device performance for this type of application, for example, as recently demonstrated for tunnel FETs used for THz detection.[69]

Other applications that can greatly profit from the excellent tunability of the band gap in Gr/hBN/BLG devices are those based on proximity-induced properties in BLG, such as superconductivity,[70,71] exchange coupling,[72] or strong spin-orbit coupling (SOC).[48] For example, by placing a strong SOC material on top of BLG, only the band associated with the layer close to the SOC material will exhibit spin splitting, thanks to the layer dependence of the bands close to the K-point (see colors in Figure 1). This makes it possible to switch on and off the spin-orbit interaction by simply switching the sign of the D-field.[48] Such an effect has been indeed recently demonstrated by taking advantage of the low disorder and the excellent control of the band gap with the applied D-field in BLG devices with graphite gates,[40] which are therefore an interesting platform for spin-orbit valves and spin transistors.[73]

Furthermore, Gr/hBN/BLG technology has allowed realizing sophisticated devices such as quantum point contacts,[32,74–76] and quantum dots in BLG with single-electron control.[77–79] This underlines the possibility of BLG as a potential host material for spin and valley qubits.[80] Moreover, thanks to a long electron phase coherence length[81] it promises to be an interesting platform for mesoscopic physics in low-dimensions.

In short, our study unambiguously shows that the Gr/hBN/BLG technology allows realizing van-der-Waals heterostructures that truly behave as semiconductors with an electrostatically tunable gap. This opens up a wide field of possible applications, especially when considering that a required scalability can also be enabled by using high quality CVD BLG material.[82–84]

Supporting Information

Supporting Information is available from the Wiley Online Library or from the author.

Acknowledgements

The authors thank S. Trellenkamp, F. Lentz, and D. Neumaier for their support in device fabrication and F. Hassler, D. Kennes, A. Garcia-Ruiz, and F. Haupt for discussions. This project has received funding from the European Union's Horizon 2020 research and innovation program under grant agreement No. 881603 (Graphene Flagship) and from the European Research Council (ERC) under grant agreement No. 820254, the Deutsche Forschungsgemeinschaft (DFG, German Research Foundation) under Germany's Excellence Strategy–Cluster of Excellence Matter and Light for Quantum Computing (ML4Q) EXC

2004/1 - 390534769, through DFG (BE 2441/9-1 and STA 1146/11-1), and by the Helmholtz Nano Facility.[85] K.W. and T.T. acknowledge support from the Elemental Strategy Initiative conducted by the MEXT, Japan (Grant Number JPMXP0112101001), and JSPS KAKENHI (Grant Numbers 19H05790, 20H00354, and 21H05233).

Open access funding enabled and organized by Projekt DEAL.

Conflict of Interest

The authors declare no conflict of interest.

Data Availability Statement

The data that support the findings of this study are openly available in Transport spectroscopy of ultraclean tunable band gaps in bilayer graphene at https://doi.org/10.5281/zenodo.6119509, reference number 6119509.

Keywords

band gap, bilayer graphene, transport spectroscopy

Received: June 4, 2022
Revised: July 9, 2022
Published online: July 27, 2022

[1] E. McCann, V. I. Fal'ko, *Phys. Rev. Lett.* **2006**, *96*, 086805.
[2] H. Min, B. Sahu, S. K. Banerjee, A. H. MacDonald, *Phys. Rev. B* **2007**, *75*, 155115.
[3] E. McCann, M. Koshino, *Rep. Prog. Phys.* **2013**, *76*, 056503.
[4] T. Ohta, A. Bostwick, T. Seyller, K. Horn, E. Rotenberg, *Science* **2006**, *313*, 951.
[5] S. Y. Zhou, G.-H. Gweon, A. V. Fedorov, P. N. First, W. A. de Heer, D.-H. Lee, F. Guinea, A. H. Castro Neto, A. Lanzara, *Nat. Mater.* **2007**, *6*, 770.
[6] K. F. Mak, C. H. Lui, J. Shan, T. F. Heinz, *Phys. Rev. Lett.* **2009**, *102*, 256405.
[7] A. B. Kuzmenko, E. van Heumen, D. van der Marel, P. Lerch, P. Blake, K. S. Novoselov, A. K. Geim, *Phys. Rev. B* **2009**, *79*, 115441.
[8] Y. Zhang, T.-T. Tang, C. Girit, Z. Hao, M. C. Martin, A. Zettl, M. F. Crommie, Y. R. Shen, F. Wang, *Nature* **2009**, *459*, 820.
[9] M. Yankowitz, J. I.-J. Wang, S. Li, A. G. Birdwell, Y.-A. Chen, K. Watanabe, T. Taniguchi, S. Y. Quek, P. Jarillo-Herrero, B. J. LeRoy, *APL Mater.* **2014**, *2*, 092503.
[10] G. R. Holdman, Z. J. Krebs, W. A. Behn, K. J. Smith, K. Watanabe, T. Taniguchi, V. W. Brar, *Appl. Phys. Lett.* **2019**, *115*, 181601.
[11] J. B. Oostinga, H. B. Heersche, X. Liu, A. F. Morpurgo, L. M. K. Vandersypen, *Nat. Mater.* **2008**, *7*, 151.
[12] B. N. Szafranek, D. Schall, M. Otto, D. Neumaier, H. Kurz, *Appl. Phys. Lett.* **2010**, *96*, 112103.
[13] F. Xia, D. B. Farmer, Y-m. Lin, P. Avouris, *Nano Lett.* **2010**, *10*, 715.
[14] B. N. Szafranek, D. Schall, M. Otto, D. Neumaier, H. Kurz, *Nano Lett.* **2011**, *11*, 2640.
[15] K. Lee, B. Fallahazad, H. Min, E. Tutuc, *IEEE Trans. Electron Devices* **2012**, *60*, 103.
[16] H. Miyazaki, K. Tsukagoshi, A. Kanda, M. Otani, S. Okada, *Nano Lett.* **2010**, *10*, 3888.
[17] J. Yan, M. S. Fuhrer, *Nano Lett.* **2010**, *10*, 4521.
[18] K. Zou, J. Zhu, *Phys. Rev. B* **2010**, *82*, 081407.
[19] T. Taychatanapat, P. Jarillo-Herrero, *Phys. Rev. Lett.* **2010**, *105*, 166601.
[20] L. Jing, V. Jairo Jr., P. Kratz, G. Liu, W. Bao, M. Bockrath, C. N. Lau, *Nano Lett.* **2010**, *10*, 4000.
[21] K. Kanayama, K. Nagashio, *Sci. Rep.* **2015**, *5*, 15789.
[22] M. R. Connolly, R. K. Puddy, D. Logoteta, P. Marconcini, M. Roy, J. P. Griffiths, G. A. C. Jones, P. A. Maksym, M. Macucci, C. G. Smith, *Nano Lett.* **2012**, *12*, 5448.
[23] R. T. Weitz, M. T. Allen, B. E. Feldman, J. Martin, A. Yacoby, *Science* **2010**, *330*, 812.
[24] M. T. Allen, J. Martin, A. Yacoby, *Nat. Commun.* **2012**, *3*, 934.
[25] J. Velasco, Y. Lee, Z. Zhao, Lei Jing, P. Kratz, Marc Bockrath, C. N. Lau, *Nano Lett.* **2014**, *14*, 1324.
[26] D.-K. Ki, V. I. Fal'ko, D. A. Abanin, A. F. Morpurgo, *Nano Lett.* **2014**, *14*, 2135.
[27] M. J. Zhu, A. V. Kretinin, M. D. Thompson, D. A. Bandurin, S. Hu, G. L. Yu, J. Birkbeck, A. Mishchenko, I. J. Vera-Marun, K. Watanabe, T. Taniguchi, M. Polini, J. R. Prance, K. S. Novoselov, A. K. Geim, M. Ben Shalom, *Nat. Commun.* **2017**, *8*, 14552.
[28] A. M. Goossens, S. C. M. Driessen, T. A. Baart, K. Watanabe, T. Taniguchi, L. M. K. Vandersypen, *Nano Lett.* **2012**, *12*, 4656.
[29] Y. Shimazaki, M. Yamamoto, I. V. Borzenets, K. Watanabe, T. Taniguchi, S. Tarucha, *Nat. Phys.* **2015**, *11*, 1032.
[30] M. Sui, G. Chen, L. Ma, W.-Y. Shan, D. Tian, K. Watanabe, T. Taniguchi, X. Jin, W. Yao, D. Xiao, Y. Zhang, *Nat. Phys.* **2015**, *11*, 1027.
[31] J. Li, K. Wang, K. J. McFaul, Z. Zern, Y. Ren, K. Watanabe, T. Taniguchi, Z. Qiao, J. Zhu, *Nat. Nanotechnol.* **2016**, *11*, 1060.
[32] H. Overweg, H. Eggimann, X. Chen, S. Slizovskiy, M. Eich, R. Pisoni, Y. Lee, P. Rickhaus, K. Watanabe, T. Taniguchi, V. Fal'ko, T. Ihn, K. Ensslin, *Nano Lett.* **2018**, *18*, 553.
[33] E. McCann, *Phys. Rev. B* **2006**, *74*, 161403.
[34] S. Slizovskiy, A. Garcia-Ruiz, A. I. Berdyugin, N. Xin, T. Taniguchi, K. Watanabe, A. K. Geim, N. D. Drummond, V. I. Fal'ko, *Nano Lett.* **2021**, *21*, 6678.
[35] A. B. Kuzmenko, L. Benfatto, E. Cappelluti, I. Crassee, D. van der Marel, P. Blake, K. S. Novoselov, A. K. Geim, *Phys. Rev. Lett.* **2009**, *103*, 116804.
[36] F. Joucken, Z. Ge, E. A. Quezada-López, J. L. Davenport, K. Watanabe, T. Taniguchi, J. Velasco, *Phys. Rev. B* **2020**, *101*, 161103.
[37] J. Jung, A. H. MacDonald, *Phys. Rev. B* **2014**, *89*, 035405.
[38] P. Kumar, Y. S. Chauhan, A. Agarwal, S. Bhowmick, *J. Phys. Chem. C* **2016**, *120*, 17620.
[39] S. Jung, N. Myoung, J. Park, T. Y. Jeong, H. Kim, K. Watanabe, T. Taniguchi, D. H. Ha, C. Hwang, H. C. Park, *Nano Lett.* **2017**, *17*, 206.
[40] J. O. Island, X. Cui, C. Lewandowski, J. Y. Khoo, E. M. Spanton, H. Zhou, D. Rhodes, J. C. Hone, T. Taniguchi, K. Watanabe, L. S. Levitov, M. P. Zaletel, A. F. Young, *Nature* **2019**, *571*, 85.
[41] Y. Zhao, P. Cadden-Zimansky, Z. Jiang, P. Kim, *Phys. Rev. Lett.* **2010**, *104*, 066801.
[42] J. Sonntag, S. Reichardt, L. Wirtz, B. Beschoten, M. I. Katsnelson, F. Libisch, C. Stampfer, *Phys. Rev. Lett.* **2018**, *120*, 187701.
[43] M. Schmitz, T. Ouaj, Z. Winter, K. Rubi, K. Watanabe, T. Taniguchi, U. Zeitler, B. Beschoten, C. Stampfer, *2D Mater.* **2020**, *7*, 041007.
[44] J. Osvald, *Solid-State Electron.* **1992**, *35*, 1629.
[45] B. I. Shklovskii, A. L. Efros, *Electronic Properties of Doped Semiconductors*, Springer-Verlag, Berlin, Germany **1984**.
[46] E. A. Henriksen, J. P. Eisenstein, *Phys. Rev. B* **2010**, *82*, 041412.
[47] A. F. Young, C. R. Dean, I. Meric, S. Sorgenfrei, H. Ren, K. Watanabe, T. Taniguchi, J. Hone, K. L. Shepard, P. Kim, *Phys. Rev. B* **2012**, *85*, 235458.
[48] J. Y. Khoo, A. F. Morpurgo, L. Levitov, *Nano Lett.* **2017**, *17*, 7003.
[49] T. Ando, *J. Phys. Soc. Jpn.* **2006**, *75*, 074716.
[50] M. Ishigami, J. H. Chen, W. G. Cullen, M. S. Fuhrer, E. D. Williams, *Nano Lett.* **2007**, *7*, 1643.
[51] J.-H. Chen, C. Jang, S. Xiao, M. Ishigami, M. S. Fuhrer, *Nat. Nanotechnol.* **2008**, *3*, 206.

[52] S. V. Morozov, K. S. Novoselov, M. I. Katsnelson, F. Schedin, D. C. Elias, J. A. Jaszczak, A. K. Geim, *Phys. Rev. Lett.* **2008**, *100*, 016602.
[53] Y. Zhang, V. W. Brar, C. Girit, A. Zettl, M. F. Crommie, *Nat. Phys.* **2009**, *5*, 722.
[54] C. R. Dean, A. F. Young, I. Meric, C. Lee, L. Wang, S. Sorgenfrei, K. Watanabe, T. Taniguchi, P. Kim, K. L. Shepard, J. Hone, *Nat. Nanotechnol.* **2010**, *5*, 722.
[55] C. Stampfer, J. Güttinger, S. Hellmüller, F. Molitor, K. Ensslin, T. Ihn, *Phys. Rev. Lett.* **2009**, *102*, 056403.
[56] P. Gallagher, K. Todd, D. Goldhaber-Gordon, *Phys. Rev. B* **2010**, *81*, 115409.
[57] A. A. Zibrov, C. Kometter, H. Zhou, E. M. Spanton, T. Taniguchi, K. Watanabe, M. P. Zaletel, A. F. Young, *Nature* **2017**, *549*, 7672.
[58] D. Rhodes, S. H. Chae, R. Ribeiro-Palau, J. Hone, *Nat. Mater.* **2019**, *18*, 541.
[59] M. Yankowitz, Q. Ma, P. Jarillo-Herrero, B. J. LeRoy, *Nat. Rev. Phys.* **2019**, *1*, 112.
[60] H. Shioya, M. Yamamoto, S. Russo, M. F. Craciun, S. Tarucha, *Appl. Phys. Lett.* **2012**, *100*, 033113.
[61] T.-T. Tang, Y. Zhang, C.-H. Park, B. Geng, C. Girit, Z. Hao, M. C. Martin, A. Zettl, M. F. Crommie, S. G. Louie, Y. R. Shen, F. Wang, *Nat. Nanotechnol.* **2010**, *5*, 32.
[62] J. Yan, M.-H. Kim, J. A. Elle, A. B. Sushkov, G. S. Jenkins, H. M. Milchberg, M. S. Fuhrer, H. D. Drew, *Nat. Nanotechnol.* **2012**, *7*, 472.
[63] M. Cheli, G. Fiori, G. Iannaccone, *IEEE Trans. Electron Devices* **2009**, *56*, 2979.
[64] S. Das, J. Appenzeller, *IEEE Trans. Nanotechnol.* **2011**, *10*, 1093.
[65] R. Sako, H. Tsuchiya, M. Ogawa, *IEEE Trans. Electron Devices* **2011**, *58*, 3300.
[66] G. Alymov, V. Vyurkov, V. Ryzhii, D. Svintsov, *Sci. Rep.* **2016**, *6*, 24654.
[67] S. S. Dhillon, M. S. Vitiello, E. H. Linfield, A. G. Davies, M. C. Hoffmann, J. Booske, C. Paoloni, M. Gensch, P. Weightman, G. P. Williams, E. Castro-Camus, D. R. S. Cumming, F. Simoens, I. Escorcia-Carranza, J. Grant, S. Lucyszyn, M. Kuwata-Gonokami, K. Konishi, M. Koch, C. A. Schmuttenmaer, T. L. Cocker, R. Huber, A. G. Markelz, Z. D. Taylor, V. P. Wallace, J. A. Zeitler, J. Sibik, T. M. Korter, B. Ellison, S. Rea et al, *J. Phys. D: Appl. Phys.* **2017**, *50*, 043001.
[68] D. A. Bandurin, D. Svintsov, I. Gayduchenko, S. G. Xu, A. Principi, M. Moskotin, I. Tretyakov, D. Yagodkin, S. Zhukov, T. Taniguchi, K. Watanabe, I. V. Grigorieva, M. Polini, G. N. Goltsman, A. K. Geim, G. Fedorov, *Nat. Commun.* **2018**, *9*, 5392.
[69] I. Gayduchenko, S. G. Xu, G. Alymov, M. Moskotin, I. Tretyakov, T. Taniguchi, K. Watanabe, G. Goltsman, A. K. Geim, G. Fedorov, D. Svintsov, D. A. Bandurin, *Nat. Commun.* **2021**, *12*, 543.
[70] R. Kraft, J. Mohrmann, R. Du, P. B. Selvasundaram, M. Irfan, U. N. Kanilmaz, F. Wu, D. Beckmann, H. von Lähneysen, R. Krupke, A. Akhmerov, I. Gornyi, R. Danneau, *Nat. Commun.* **2018**, *9*, 2041.
[71] J. Li, H.-B. Leng, H. Fu, K. Watanabe, T. Taniguchi, X. Liu, C.-X. Liu, J. Zhu, *Phys. Rev. B* **2020**, *101*, 195405.
[72] K. Zollner, M. Gmitra, J. Fabian, *Phys. Rev. Lett.* **2020**, *125*, 196402.
[73] M. Gmitra, J. Fabian, *Phys. Rev. Lett.* **2017**, *119*, 146401.
[74] R. Kraft, I. V. Krainov, V. Gall, A. P. Dmitriev, R. Krupke, I. V. Gornyi, R. Danneau, *Phys. Rev. Lett.* **2018**, *121*, 257703.
[75] L. Banszerus, B. Frohn, T. Fabian, S. Somanchi, A. Epping, M. Müller, D. Neumaier, K. Watanabe, T. Taniguchi, F. Libisch, B. Beschoten, F. Hassler, C. Stampfer, *Phys. Rev. Lett.* **2020**, *124*, 177701.
[76] Y. Lee, A. Knothe, H. Overweg, M. Eich, C. Gold, A. Kurzmann, V. Klasovika, T. Taniguchi, K. Wantanabe, V. Fal'ko, T. Ihn, K. Ensslin, P. Rickhaus, *Phys. Rev. Lett.* **2020**, *124*, 126802.
[77] M. Eich, R. Pisoni, H. Overweg, A. Kurzmann, Y. Lee, P. Rickhaus, T. Ihn, K. Ensslin, F. Herman, M. Sigrist, K. Watanabe, T. Taniguchi, *Phys. Rev. X* **2018**, *8*, 031023.
[78] L. Banszerus, B. Frohn, A. Epping, D. Neumaier, K. Watanabe, T. Taniguchi, C. Stampfer, *Nano Lett.* **2018**, *18*, 4785.
[79] L. Banszerus, S. Möller, E. Icking, K. Watanabe, T. Taniguchi, C. Volk, C. Stampfer, *Nano Lett.* **2020**, *20*, 2005.
[80] G. Y. Wu, N.-Y. Lue, Y.-C. Chen, *Phys. Rev. B* **2013**, *88*, 125422.
[81] S. Engels, B. Terrés, A. Epping, T. Khodkov, K. Watanabe, T. Taniguchi, B. Beschoten, C. Stampfer, *Phys. Rev. Lett.* **2014**, *113*, 126801.
[82] L. Liu, H. Zhou, R. Cheng, W. J. Yu, Y. Liu, Y. Chen, J. Shaw, X. Zhong, Y. Huang, X. Duan, *ACS Nano* **2012**, *6*, 8241.
[83] M. Schmitz, S. Engels, L. Banszerus, K. Watanabe, T. Taniguchi, C. Stampfer, B. Beschoten, *Appl. Phys. Lett.* **2017**, *110*, 263110.
[84] T. Bisswanger, Z. Winter, A. Schmidt, F. Volmer, K. Watanabe, T. Taniguchi, C. Stampfer, B. Beschoten, *Nano Lett.* **2022**, *22*, 4949.
[85] W. Albrecht, J. Moers, B. Hermanns, *J. Large-Scale Res. Facil.* **2017**, *3*, 112.